The Astrophysical Journal Letters, 959:L4 (8pp), 2023 December 10 https://doi.org/10.3847/2041-8213/ad00bd

Time-dependent Dynamics of the Corona

Emily I. Mason[1], Roberto Lionello[1], Cooper Downs[1], Jon A. Linker[1], Ronald M. Caplan[1], and Marc L. DeRosa[2]
[1] Predictive Science Inc., 9990 Mesa Rim Rd., Ste. 170, San Diego, CA 92121, USA; emason@predsci.com
[2] Lockheed Martin Solar and Astrophysics Laboratory, 3251 Hanover Street B/203, Palo Alto, CA 94304, USA

Received 2023 July 12; revised 2023 August 30; accepted 2023 August 30; published 2023 December 8

Abstract

We present in this Letter the first global comparison between traditional line-tied steady-state magnetohydrodynamic models and a new, fully time-dependent thermodynamic magnetohydrodynamic simulation of the global corona. To approximate surface magnetic field distributions and magnitudes around solar minimum, we use the Lockheed Evolving Surface-Flux Assimilation Model to obtain input maps that incorporate flux emergence and surface flows over a full solar rotation, including differential rotation and meridional flows. Each time step evolves the previous state of the plasma with a new magnetic field input boundary condition, mimicking photospheric driving on the Sun. We find that this method produces a qualitatively different corona compared to steady-state models. The magnetic energy levels are higher in the time-dependent model, and coronal holes evolve more along the following edge than they do in steady-state models. Coronal changes, as illustrated with forward-modeled emission maps, evolve on longer timescales with time-dependent driving. We discuss implications for active and quiet Sun scenarios, solar wind formation, and widely used steady-state assumptions like potential field source surface calculations.

Unified Astronomy Thesaurus concepts: Solar magnetic flux emergence (2000); Solar magnetic fields (1503); Magnetohydrodynamical simulations (1966); Quiet solar corona (1992); Solar corona (1483); Solar extreme ultraviolet emission (1493)

Supporting material: animation

1. Introduction

The solar corona's structure and much of its evolution are both ultimately determined by the magnetic field at the photosphere. Phenomena such as plasma flows and magnetic reconnection are driven by changes rooted at the solar surface; effects of these dynamics propagate into the corona, interacting in a delicate balance and—sometimes—explosive loss of balance between the various forces. Remote sensing observations help researchers track and unravel many aspects of coronal dynamics, but they are often insufficient to fully understand the interplay of plasma and the magnetic field. There are many factors for this: a lack of full-Sun coverage of the evolving surface magnetic fields, the difficulties inherent in measuring coronal magnetic fields directly (e.g., Dima & Schad 2020), an incomplete understanding of the solar dynamo (Usoskin 2023, and references therein), the enormous range of scales at which critically important phenomena occur in the corona (Klimchuk 2006; Marsch 2006; Guidoni et al. 2016), among others. In order to delve more deeply into the mechanisms that drive coronal dynamics, we turn to models.

Magnetohydrodynamic (MHD) models of the global solar corona generally involve two elements. First a full map of the radial magnetic field, B_r, in the photosphere is used set the magnetic boundary condition at the coronal base. Second, the MHD model is advanced to evolve the plasma and coronal magnetic fields until they reach a near-equilibrium state (e.g., Mikić et al. 1999; Roussev et al. 2003; Riley et al. 2006; Réville et al. 2020). The input magnetic map is usually static in time, constituting the so-called steady-state (SS) solution. In this case, any evolution is either due to relaxation or true coronal processes. However, when investigating large-scale dynamics over days or weeks, the time evolution of surface fields introduces long-period solar phenomena that are generally neglected. These include solar differential rotation and meridional flows, as well as global patterns of flux emergence and dispersion (and the more localized emergence and evolution of solar active regions). Several previous studies have incorporated aspects of time dependence; the work of Yeates et al. (2007; continued in Yeates et al. 2008 and Yeates & MacKay 2009), for example, incorporated flux emergence and dispersion, but this was implemented in a magnetofrictional model composed of a series of relaxations. Yang et al. (2012) used daily updated Michelson Doppler Imager data as the initial data input for a long-term MHD model. Hayashi et al. (2022) use a field-matching relaxation technique based on vector magnetograms, to emulate time dependence. However, neither of these latter models included thermodynamics. The model presented here, as explained in more detail in the following section, combines purely simulated time-evolving magnetic field boundary conditions with thermodynamic MHD.

We have recently reported this time-dependently driven thermodynamic MHD simulation of the global corona covering roughly one month of coronal evolution (Lionello et al. 2023). In this Letter, we present a comparison of the time-dependent model with corresponding SS models run using the same B_r boundary conditions. We find that the introduction of time dependence has a significant effect on low-coronal dynamics, which is also apparent in the simulated emission.

In Section 2 we provide a brief overview of the model and its capabilities, as well as details of the runs. Section 3 presents the results of the simulations and some relevant visualizations. In the final section, we discuss what these findings mean for interpreting solar observations and for common SS extrapolations.

2. MAS

For our global coronal MHD calculations we employ the Magnetohydrodynamic Algorithm outside a Sphere (MAS) model. MAS solves the thermodynamic, resistive MHD equations on a nonuniform, nonadaptive spherical mesh in the Carrington frame; these equations contain coronal heating, thermal conduction parallel to field, and radiative losses. It uses a semi-implicit time-stepping algorithm, and covers the global corona and solar wind to 30 $R_\odot$ (e.g., Mikić et al. 1999; Riley et al. 2011; Lionello et al. 2013). A wave-turbulence-driven (WTD) approach is applied for coronal heating and solar wind acceleration to model the large-scale solar wind properties (Lionello et al. 2014; Downs et al. 2016). A description of the equations solved and boundary conditions used for the thermodynamic MHD approach is fully described in Appendix A of Török et al. (2018). A description of the auxiliary equations solved for the MAS-WTD model is provided in the methods section of Mikić et al. (2018).

The thermodynamic MHD approach allows the plasma density and temperature to be computed with sufficient accuracy to forward model EUV and soft X-ray emission and other remote sensing observables (e.g., Lionello et al. 2009; Downs et al. 2010, 2013). MAS has produced state-of-the-art solutions of the corona for eclipses (Mikić et al. 2018; Boe et al. 2021, 2022), coronal mass ejections (Lionello et al. 2013; Török et al. 2018; Downs et al. 2021), and the inner heliosphere in general (Riley et al. 2011, 2019). Past eclipse prediction work with MAS, in particular, has shown its flexibility with generating various simulated emission quantities in forms that are easily comparable to observations.

While quasi-steady models provide a baseline description of the solar corona, remote solar and in situ observations over the last two decades indicate that the solar wind is always dynamically evolving (Rouillard et al. 2010a, 2010b; Kepko et al. 2016). A significant new capability has recently been added to the MAS code, detailed in (Lionello et al. 2023): the ability to model the time-evolving corona in response to global photospheric magnetic flux evolution. While we lack global observations of the Sun's surface field, flux transport models (Wang & Sheeley 1994; Worden & Harvey 2000; Schrijver & DeRosa 2003; Arge et al. 2010; Upton & Hathaway 2013) provide us a with a sequence of global maps, as well as the underlying flows that transported the fields on the solar surface. This information can be used to drive the global coronal MHD simulation in time, and here we briefly outline a few of the salient details. The flux transport model used here includes differential rotation, meridional flows, convective dispersal, and photospheric flux emergence and decay. The evolving maps of the photospheric field were generated by a run of the Lockheed Evolving Surface-Flux Assimilation Model (Schrijver & DeRosa 2003), where a "synthetic" Sun is simulated, with the evolving surface fields scaled and distributed such that they approximate the conditions near solar minimum. In this calculation, bipolar flux emergence that spans the scales of ephemeral regions to active regions is controlled via an automated process that randomly selects values for flux, location, and axial tilt based in power-law distributions derived from long-term observational statistics. The numerous smaller bipoles collectively create a realistic, evolving distribution of random flux on the full-Sun surface. The largest bipoles (active regions) are emerged over a few days as collection of smaller bipoles that collectively match the overall flux of the region but interact individually.

The MHD calculations used here were run with a resolution of 269 cells in r, 181 cells in θ, and 361 cells in ϕ, and span the global corona from 1–30 $R_\odot$. The time-dependent MHD calculation is driven at the inner boundary for 30 days of physical evolution using electric fields derived from a sequence of 720 full-Sun B_r maps (1 hr cadence) and the differential rotation and meridional flow profiles obtained from the flux transport calculation. MAS handles the time-dependent driving via a decomposition of the tangential electric field at the inner boundary into two potentials,

$$\boldsymbol{E}_{t0} = \nabla_t \times \Psi \hat{\boldsymbol{r}} + \nabla_t \Phi, \qquad (1)$$

one of which is governed entirely by the radial magnetic field there ($\nabla_t^2 \Psi = \frac{\partial B_r}{\partial t}$), and the other of which is governed by the flows that are known from the flux transport maps ($\nabla_t^2 \Phi = -\nabla_t \cdot (\boldsymbol{v} \times \boldsymbol{B})_t$). The remaining component of the electric field, $\boldsymbol{E}_r$, a self-consistent treatment of the perpendicular boundary flows, and limiting truncations are obtained from an ideal MHD assumption ($\boldsymbol{E} \cdot \boldsymbol{B} \sim 0$). For further details of the flows and the specifications of the time-dependent driving, the reader is encouraged to read Lionello et al. (2023), as previously noted.

3. Results

3.1. Global Evolution

For this study, we compare the time-dependent corona (TDC) simulation with 12 analogous SS simulations. The SS model runs are generated using snapshots of the full-Sun surface B_r at various stages in the TDC model, spaced at a cadence of 15 hr between 440 and 620 hr (inclusive). Figure 1(a) shows an example time step from the TDC run in two projections: on the left, a simulated Earth view of forward-modeled 211 Å emission from the Atmospheric Imaging Assembly (AIA; Lemen et al. 2012), which is line-of-sight (LOS) integrated along the plane of the sky. On the right, we show a latitude-longitude map of the same AIA observable in Carrington coordinates, similar to a Mercator projection, where the LOS integration is instead along the radial direction. We use the AIA 193 or 211 Å channels for all of the EUV data in this Letter. The SS simulation parameters were identical to the TDC run in all respects except for the evolution of the boundary conditions. The SS runs simulate just over 80 hr of coronal evolution, which is sufficient for the simulations to relax fully.

Figure 1(b) shows two-layer maps for a sequence of time steps showing particularly rapid evolution. The red and blue map is the photospheric magnetic flux, while the orange and purple map shows the difference in simulated EUV 211 Å emission between the TDC and SS simulations of the same B_r map. Orange delineates more SS emission (i.e., the TDC model is darker), while purple indicates the opposite. We will discuss the subregion with the high concentration of purple shortly; however, overall there is significantly more orange in the maps, particularly at the edges of coronal hole boundaries, consistent

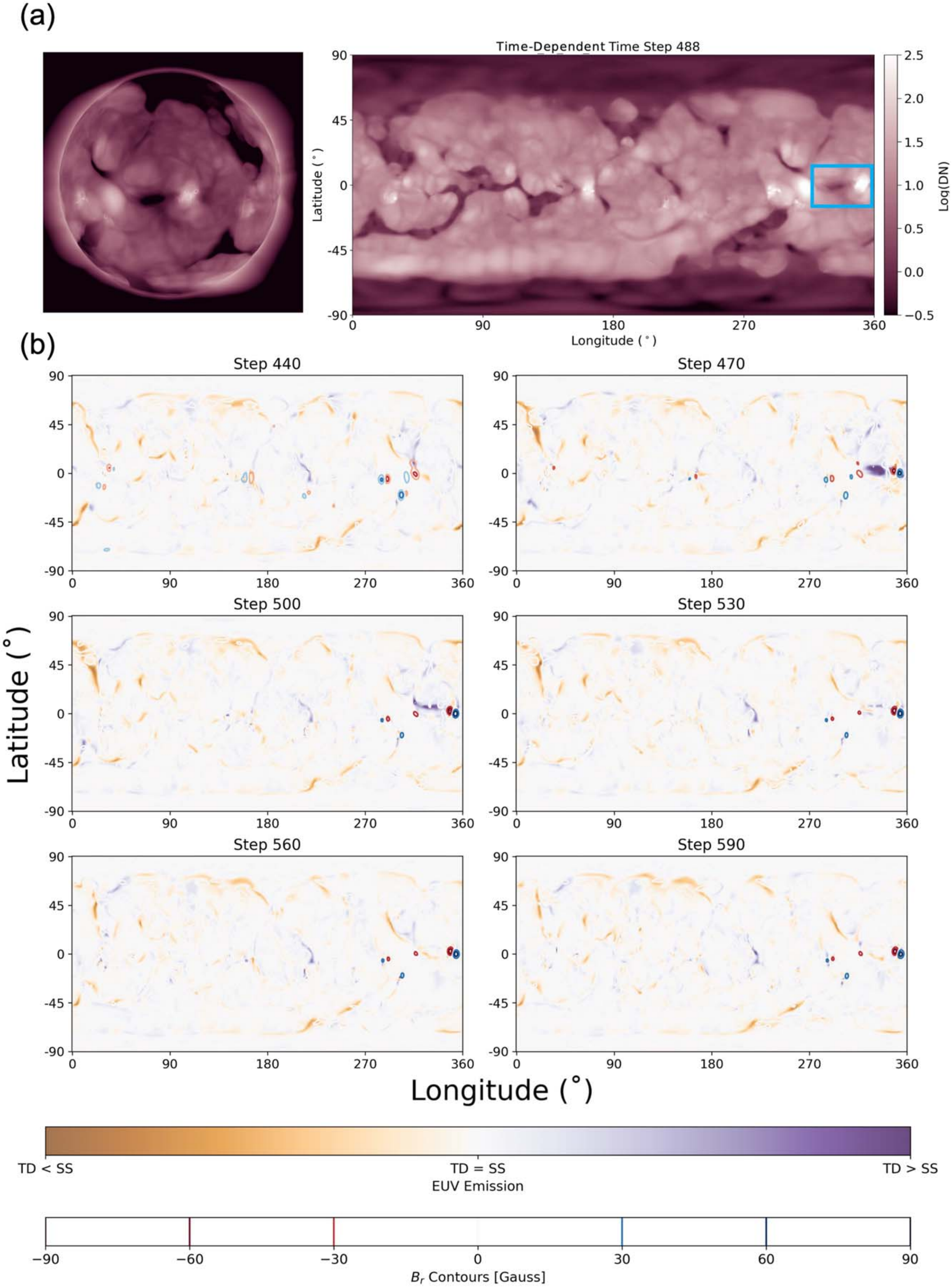

Figure 1. (a) Left: forward-modeled emission image for the AIA 211 Å channel at time step 488. Right: the corresponding full-Sun map of AIA 211 Å emission, integrated along the radial direction. The region highlighted in blue is the subregion considered in the second half of this Letter. (b) Plots of B_r and AIA 211 Å differenced emission; the latter color table highlights where the TDC simulation emission is higher (purple) and where the SS simulations' emission is higher (orange).

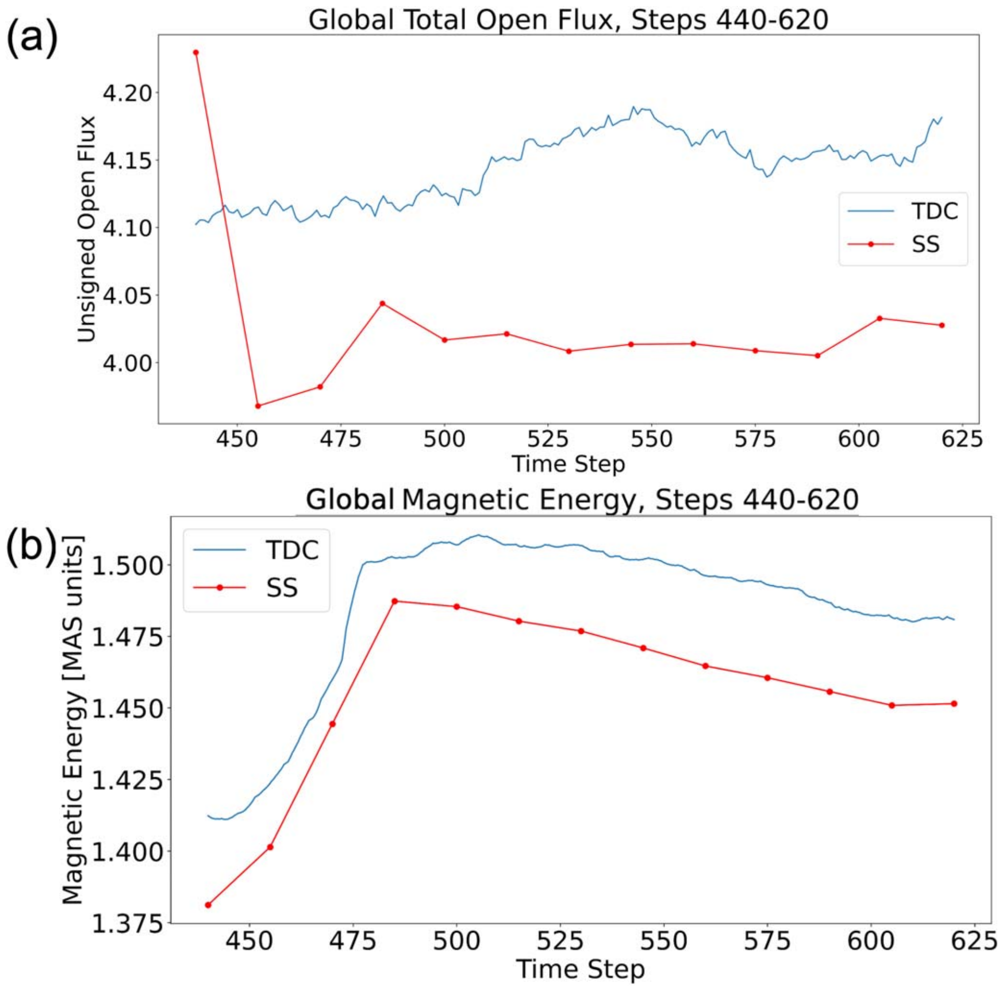

Figure 2. (a) Percent of global total open flux for SS and TDC during the selected time period. Except for time step 440, immediately before the emergence of the active region, the SS has uniformly less open flux than the TDC simulation. (b) The global magnetic energy for both the TDC and SS simulations.

with the TDC simulation having a higher proportion of open magnetic flux.

Direct open flux calculations support this implication. As seen in Figure 2(a), for all time steps in this interval except the first (which occurs immediately before these dynamics begin), the TDC simulations consistently exhibit more open flux globally than the SS simulation. The additional drivers introduced via the boundary conditions for the TDC simulation drive higher rates of interchange reconnection on a global scale. It also introduces more magnetic energy, as seen in Figure 2(b). This is in contrast to the region of interest (ROI) upon which we focus for the remainder of this Letter, where there is less open flux locally in the TDC simulation. In particular, we study the period of 180 hr between 440 and 620, which corresponds to the period of greatest flux emergence and the subsequent coronal rearrangements. In the next section, we consider these dynamics in a more specific region.

3.2. Region of Interest Evolution

We now study the region highlighted in blue in the right panel of Figure 1(a) in greater depth (referred to as the region of interest or ROI hereafter); during the period of hours 440–620 of the full TDC simulation, a large active region emerges and a coronal hole extension enlarges significantly. Figure 3 shows the open flux evolution in the ROI during this period. We masked a rectangular area (the same area shown in blue in Figure 1(a)) that encompassed the expansion of the coronal hole; the SS runs exhibit more open flux faster than the TDC simulation, which shows a slow but steady increase in the (negatively oriented) open flux. Later in the evolution, the two simulations come into better agreement, with the final state values being very similar. This tendency for a significant time lag in the TDC simulation is echoed in the EUV results from Figure 1.

The emergence of the coronal hole in the TDC simulation is presented in Figure 4 (an animation showing the full time period is available in the digital version of this Letter). The visualizations show the B_r at the photosphere, a spherical slice of forward-modeled 193 Å emission at 1.3 $R_\odot$ to show the coronal hole darkening, and field lines plotted within the ROI. The field lines stretch for roughly two days of solar time while remaining closed; the majority of this magnetic field becomes open (and correspondingly darkens in the simulated EUV) only approximately 50 hr after the active region emerges, while some of the field lines that eventually open remain closed for over 100 hr.

To examine the global differences between the two simulation approaches, we produced difference maps that differentiated between agreement among the TDC and SS maps, and each possible type of disagreement. These difference maps are shown in Figure 5. The various shades of black and

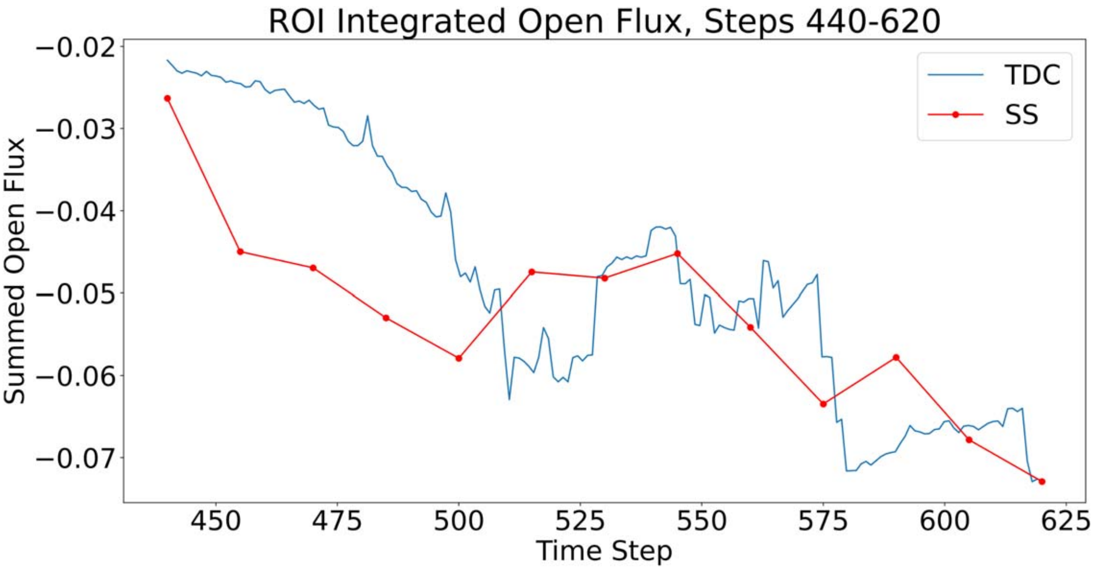

Figure 3. Comparison of the signed net open fluxes for both cases within the region highlighted with the blue rectangle in Figure 5. This captures the early evolution of the negative-polarity coronal hole; note how rapidly the steady-state cases show open flux in the region of interest during the early emergence of the active region, while the time-dependent case does not reach similar levels for up to 50 hr later.

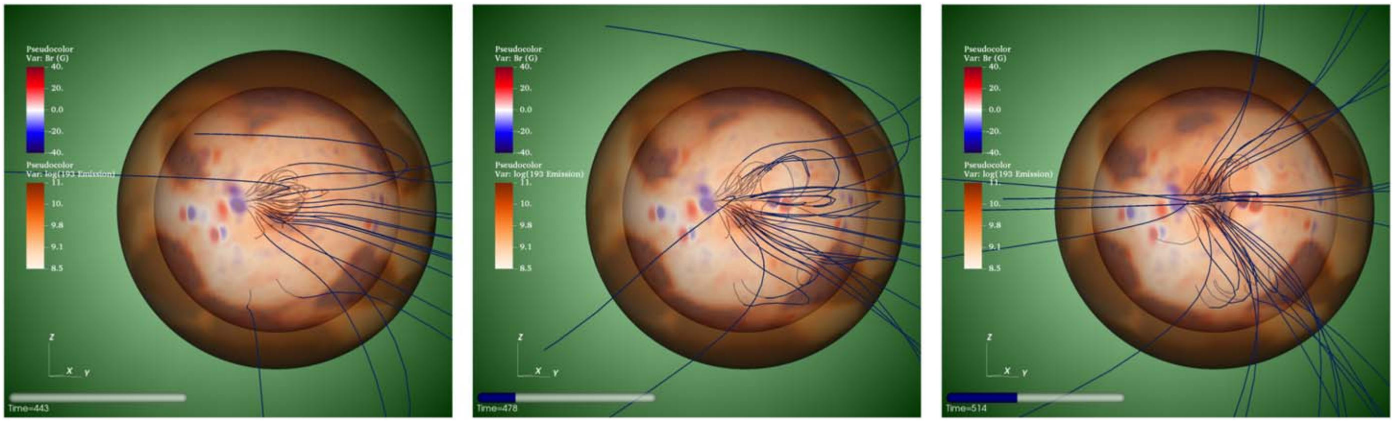

Figure 4. Visualization of B_r, simulated 193 Å emission at 1.3 $R_\odot$, and magnetic field lines throughout the region of the emerging CH. The time stamps correspond to hours after the beginning of the simulation. Most of the field lines stretch but remain closed for over 40 hr, while some do not open until nearly 80 hr after the emergence begins.

(An animation of this figure is available.)

gray exhibit the open field regions for the negative polarity, while the shades of red do the same for the positive polarity. There are two important trends in the disagreement between the models: first, there is a persistent pattern of increased open field in the TDC along the eastern side of most equatorial coronal hole (CH) extensions, and increased open field in the SS along the western side. We term this pattern persistent, since it does not change greatly with time. The second trend can be seen in the ROI (highlighted with the blue rectangle). Here, the difference between the TDC and SS is significant and time-dependent, during the period of active region emergence and CH expansion. The black shows where the SS model has already expanded to the full extent of the CH; this region slowly fills in with medium gray, as the TDC model's field opens up and aligns with the SS field. The right column shows the same map projected onto a sphere, centered on the ROI and with field lines from both the SS and TDC models to show how the fields change in 3D during this evolution.

4. Discussion and Conclusions

In this paper, we compare a TDC coronal simulation with a series of SS simulations using the same boundary conditions. The time-dependent corona results presented here include differential rotation, meriodional flows, and flux emergence and decay. The photospheric flux distribution and corresponding evolution that drive the TDC model at 1 hr cadence is roughly consistent with the conditions near solar minimum. In this particular TDC run, the B_r evolution is matched exactly, and we observe that the TDC run contains slightly more magnetic energy overall, which can only be due to the driving process. This is the primary driver of the increased open flux seen in the TD simulation. However, we do not leverage the freedom to emerge additional transverse fields and inject additional helicity along or near polarity inversion lines (Cheung & DeRosa 2012; Mikić et al. 2018). Instead all evolution was due solely to the global motions and local

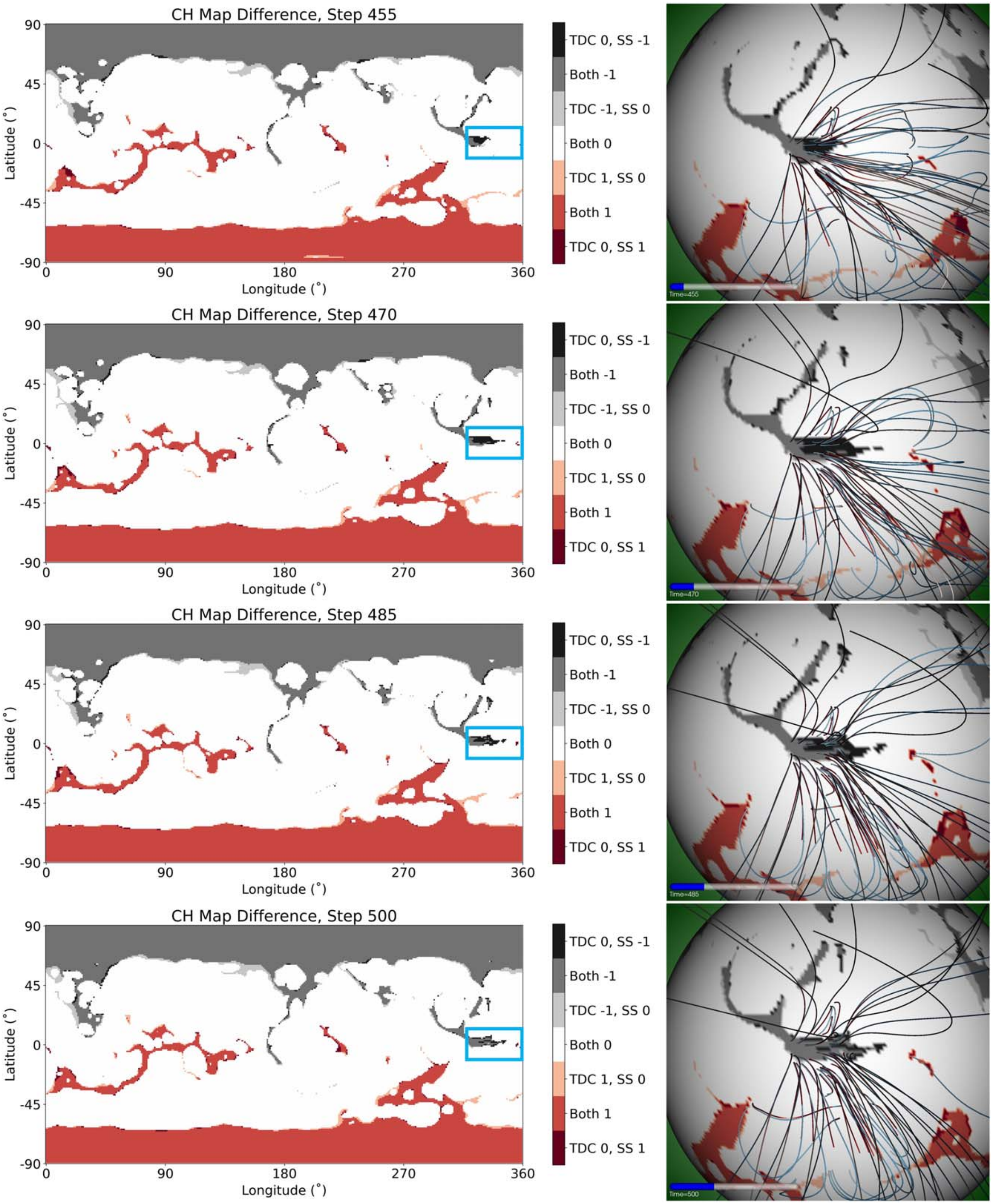

Figure 5. Left: difference maps showing agreement and disagreement between the steady-state (SS) and time-dependent runs. Black corresponds to locations where the SS is open (negative-polarity CH) but the TDC is closed, medium gray is where both are open (negative polarity), light gray is where the TDC is open (negative polarity) but the SS is closed, white is where both are closed, pink is where TDC is open (positive polarity) but the SS is closed, red is where both are open (positive polarity), and maroon is where the TDC is closed but the SS is open (positive polarity). The blue rectangle on each map shows the region integrated over for Figure 3. Right: 3D visualizations of the same maps at the same times, with the SS field lines in red/orange and the TDC field lines in shades of blue. The seed locations of the field lines are the same for both models, and black lines are open for both SS and TDC.

emergence/cancellation of the radial field, making it effectively a "minimal" case for magnetic energy injected by driving.

To compare the differences imposed by the time-dependent model during a period of flux emergence and nearby open flux evolution, we used the same B_r files for 15 evenly spaced time steps to run SS simulations. These SS simulations were fully relaxed, but inherently lacked the magnetic "history" of the time-dependent simulation; this was evident in systematically divergent coronal hole boundaries on the global scale, and in a time lag for localized open flux evolution on the scale of several days.

The time-dependent simulation exhibits significant temporal lags in magnetic field evolution, which affects both the local and global structure. These results show that even slow driving with relatively weak fields at the model's lower boundary leads to in several-day time differences for the open magnetic fluxes. It is particularly worth noting that the enhanced magnetic energy, while contributing to consistently greater open flux on a global scale, does not necessarily translate to rapidly opening flux on a local scale. This is most clearly seen in the coronal hole region focused on in Section 3.2. The time lags observed here would significantly impact spacecraft connectivity calculations, modeling of corotating interaction region creation, and the results of solar energetic particle propagation modeling; this makes a strong argument for incorporating time-dependent driving more broadly into simulations, especially solar wind propagation models.

In the same vein, for applications such as solar wind and space weather predictions, this shows that potential-field source surface (PFSS) extrapolations, which are derived from a single "snapshot" of magnetic information may fail to represent the instantaneous structure of the corona at any moment in time. Instead, we found that the corona evinces magnetic hysteresis, where the magnetic field takes a considerable amount of time to adjust to a new configuration. A field that has been closed lengthens greatly before it opens, and this stretching can take many hours. These intermediate states, which likely constitute most of the corona for significant proportions of the solar cycle, cannot be modeled simply through an instantaneous field with no consideration of the previous state. It remains to be seen to what degree the time lag scales with the strength of emergent magnetic flux; as previously noted, the emerging fields in this simulation were not particularly strong, and arguments could be made for stronger fields to generate either faster or slower evolution. We hypothesize that the corona responds to photospheric driving at different rates depending upon the local topology: the presence of a nearby null point could bias the system toward faster evolution through ready interchange reconnection, while strong overlying fields connecting preexisting active regions or the closed field of a helmet streamer may retard evolution. In order to more accurately capture the time-dependent effects in the corona discussed here, PFSS extrapolations could be adjusted to utilize a short time series of magnetic field maps and a method to interpolate the evolution between them, rather than the currently common method using a single photospheric input in time.

In addition to these hysteresis effects, there were other major differences between the SS and TDC runs along the open/closed boundary for all of the associated time steps that affect traditional single-map views of open flux. Locally to the ROI, these differences serve to illustrate the significant delay in open flux evolution in the expanding coronal hole between the SS and TDC runs, as discussed above. However, the global pattern that the TDC runs exhibit, with greater open flux on the eastern coronal hole boundaries and less on the western boundaries, constitutes consistent and strong evidence of interchange reconnection driven by the differential rotation (as popularly theorized by, e.g., Lionello et al. 2005, and references therein). In future simulations we plan to enhance the resolution around an open/closed boundary and study in more detail how the magnetic field and boundary evolve using tools such as the slip-back mapping method (Lionello et al. 2005; Titov et al. 2009). We will also explore the role of additional helicity injection and shear on the global coronal state. Such experiments and the use of forward modeling and observational diagnostics such as coronal hole detection and correlation dimension mapping (Mason & Uritsky 2022) will help further elucidate the role of interchange reconnection in the global corona.

Taken together, the combination of regional hysteresis and widespread constant boundary evolution shows that *time dependence is important for coronal analysis on any scale and for all structures*. The quiet and active corona alike are affected by the reconnection (or suppression thereof) exhibited by the dynamics captured here. The structure of coronal holes affects the shape and evolution of the helmet streamers by which they are connected. This, in turn, modulates the processing of magnetic field throughout the small-scale quiet Sun in the low corona to the large-scale closed regions above (Morosan et al. 2020; Liu & Su 2021; Schlenker et al. 2021; Scott et al. 2021). While the total open flux for the TDC run was only greater by a few percent, that few percent is concentrated in a few narrow areas along open/closed boundaries, heightening its influence there. Furthermore, as seen in the ROI highlighted here, short-term evolution like the emergence of an active region can distort local fields rapidly, while the end-result structural changes (i.e., the expansion of the coronal hole) do not occur until days later. All of these aspects contribute to the background state of the global corona at any given time. This has major implications for impulsive events like flares and prominence eruptions, despite the fact that the timescales of such events are too short to be directly affected by global details like differential rotation. Ultimately, the actual corona is evolving continuously in response to photospheric evolution: modeling that aims to explore magnetic field structure and evolution will benefit from being time-dependent as well.

Acknowledgments

This work was supported by the NASA Heliophysics Living With a Star Science and Strategic Capabilities programs (grant Nos. 80NSSC20K0192, 80NSSC22K1021, and 80NSSC22K0893), the NASA Heliophysics System Observatory Connect program (grant No. 80NSSC20K1285), and the NSF PREEVENTS program (grant ICER1854790). Computing resources supporting this work were provided by the NASA High-End Computing (HEC) Program through the NASA Advanced Supercomputing (NAS) Division at Ames Research Center and by the Expanse supercomputer at the San Diego Supercomputing Center through the NSF ACCESS and XSEDE programs. M.L.D. acknowledges support from NASA under contract NNG04EA00C as part of the AIA science team.

ORCID iDs

Emily I. Mason https://orcid.org/0000-0002-8767-7182
Roberto Lionello https://orcid.org/0000-0001-9231-045X
Cooper Downs https://orcid.org/0000-0003-1759-4354
Jon A. Linker https://orcid.org/0000-0003-1662-3328

Ronald M. Caplan https://orcid.org/0000-0002-2633-4290
Marc L. DeRosa https://orcid.org/0000-0002-6338-0691

References

Arge, C., Henney, C., Koller, J., et al. 2010, in Twelfth Int. Solar Wind Conf. 1216, ed. M. Maksimovic, 343
Boe, B., Habbal, S., Downs, C., & Druckmüller, M. 2021, ApJ, 912, 44
Boe, B., Habbal, S., Downs, C., & Druckmüller, M. 2022, ApJ, 935, 173
Cheung, M. C. M., & DeRosa, M. L. 2012, ApJ, 757, 147
Dima, G. I., & Schad, T. A. 2020, ApJ, 889, 109
Downs, C., Linker, J. A., Mikić, Z., et al. 2013, Sci, 340, 1196
Downs, C., Lionello, R., Mikić, Z., Linker, J. A., & Velli, M. 2016, ApJ, 832, 180
Downs, C., Roussev, I. I., van der Holst, B., et al. 2010, ApJ, 712, 1219
Downs, C., Warmuth, A., Long, D. M., et al. 2021, ApJ, 911, 118
Guidoni, S. E., DeVore, C. R., Karpen, J. T., & Lynch, B. J. 2016, ApJ, 820, 60
Hayashi, K., Wu, C.-C., & Liou, K. 2022, ApJ, 940, 82
Kepko, L., Viall, N. M., Antiochos, S. K., et al. 2016, GeoRL, 43, 4089
Klimchuk, J. A. 2006, SoPh, 234, 41
Lemen, J. R., Title, A. M., Akin, D. J., et al. 2012, SoPh, 275, 17
Lionello, R., Cooper, D., Mason, E. I., et al. 2023, ApJ, in press, arXiv:2306.12551
Lionello, R., Downs, C., Linker, J. A., et al. 2013, ApJ, 777, 76
Lionello, R., Linker, J. A., & Mikić, Z. 2009, ApJ, 690, 902
Lionello, R., Riley, P., Linker, J. A., & Mikić, Z. 2005, ApJ, 625, 463
Lionello, R., Velli, M., Downs, C., Linker, J. A., & Mikić, Z. 2014, ApJ, 796, 111
Liu, T., & Su, Y. 2021, ApJ, 915, 55
Marsch, E. 2006, LRSP, 3, 1
Mason, E. I., & Uritsky, V. M. 2022, ApJL, 937, L19
Mikić, Z., Downs, C., Linker, J. A., et al. 2018, NatAs, 2, 913
Mikić, Z., Linker, J. A., Schnack, D. D., Lionello, R., & Tarditi, A. 1999, PhPl, 6, 2217
Morosan, D. E., Palmerio, E., Lynch, B. J., & Kilpua, E. K. J. 2020, A&A, 633, A141
Réville, V., Velli, M., Panasenco, O., et al. 2020, ApJS, 246, 24
Riley, P., Downs, C., Linker, J. A., et al. 2019, ApJL, 874, L15
Riley, P., Linker, J. A., Mikić, Z., et al. 2006, ApJ, 653, 1510
Riley, P., Lionello, R., Linker, J. A., et al. 2011, SoPh, 274, 361
Rouillard, A. P., Davies, J. A., Lavraud, B., et al. 2010a, JGRA, 115, 4103
Rouillard, A. P., Lavraud, B., Davies, J. A., et al. 2010b, JGRA, 115, 4104
Roussev, I. I., Gombosi, T. I., Sokolov, I. V., et al. 2003, ApJL, 595, L57
Schlenker, M. J., Antiochos, S. K., MacNeice, P. J., & Mason, E. I. 2021, ApJ, 916, 115
Schrijver, C., & DeRosa, M. 2003, SoPh, 212, 165
Scott, R. B., Pontin, D. I., Antiochos, S. K., DeVore, C. R., & Wyper, P. F. 2021, ApJ, 913, 64
Titov, V. S., Forbes, T. G., Priest, E. R., Mikić, Z., & Linker, J. A. 2009, ApJ, 693, 1029
Török, T., Downs, C., Linker, J. A., et al. 2018, ApJ, 856, 75
Upton, L., & Hathaway, D. H. 2013, ApJ, 780, 5
Usoskin, I. G. 2023, LRSP, 20, 2
Wang, Y. M., & Sheeley, N. R. J. 1994, ApJ, 430, 399
Worden, J., & Harvey, J. 2000, SoPh, 195, 247
Yang, L. P., Feng, X. S., Xiang, C. Q., et al. 2012, JGRA, 117, A08110
Yeates, A. R., & MacKay, D. H. 2009, SoPh, 254, 77
Yeates, A. R., MacKay, D. H., & Van Ballegooijen, A. A. 2007, SoPh, 245, 87
Yeates, A. R., MacKay, D. H., & Van Ballegooijen, A. A. 2008, SoPh, 247, 103